

Supplementary Material

An efficient titanomaghmite MOF-derived catalyst for Reverse Water Gas Shift

Orxan Sayidov^a, Luis Garzon-Tovar^a, Javier Patarroyo^b, Giazi Bekmukhamedov^b, Joseph A. Stewart^c, Bart D. Vandegehuchte^c, Nicolas Montroussier^d, Javier Ruiz-Martinez^b, Jorge Gascon^{a*}

^a Advanced Catalytic Materials (ACM), KAUST Catalysis Center (KCC), King Abdullah University of Science and Technology (KAUST), Thuwal 23955-6900, Saudi Arabia

^b KAUST Catalysis Center, King Abdullah University of Science and Technology, Jeddah, Saudi Arabia

^c TotalEnergies OneTech Belgium, Zone Industrielle Feluy C, Seneffe, 7181, Belgium

^d TotalEnergies OneTech, Tour Coupole, 2 place Jean Millier, La Défense 6, 92078, Paris La Défense cedex, France

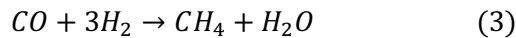
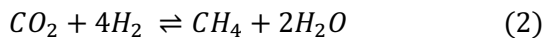
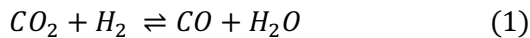
Contents

1.	Experimental Section.....	3
1.1	Kinetic Model for CO ₂ Hydrogenation	3
1.2	Process simulation.....	4
1.3	Formula determination of the catalyst.....	4
2.	Supplementary Figures.....	5
2.1	Characterization of MIL-88B (Fe, Ti)	5
2.2	Characterization of FeTi@C materials	7
2.3	Characterization of Spent Catalysts	19
2.4	Catalytic Results.....	23
2.5	Kinetic Study Results	29
3.	Supplementary Tables	32
4.	References	34

1. Experimental Section

1.1 Kinetic Model for CO₂ Hydrogenation

The kinetic study was done to determine rate equations that fit experimental data behind RWGS activity on FeTi@C550-5 catalyst. For kinetic analysis, previously proposed kinetic models that included RWGS (eq. 1), Sabatier reaction (eq. 2) and CO methanation (eq. 3) were tested:



To operate at kinetic regime the experimental data was obtained at CO₂ conversion levels up to 10%. The kinetic constants are defined from reparametrized Arrhenius equation of as below (eq. 11):

$$k_j = k_j^0 \left[-\frac{Ea_j}{R} \left(\frac{1}{T} - \frac{1}{T_0} \right) \right] \quad (4)$$

Where k_j^0 is the kinetic constant of reaction j at T_0 reference temperature of 665 K, Ea_j is the apparent activation energy of corresponding reaction, R and T are universal gas constant and reaction temperature respectively. Similarly, K_i adsorption constants of components were found from reparametrized van't Hoff equation as below (eq. 12):

$$K_i = K_i^0 \exp \left[-\frac{\Delta H_i}{R} \left(\frac{1}{T} - \frac{1}{T_0} \right) \right] \quad (5)$$

Where K_i^0 is the adsorption constant of component i at T_0 reference temperature and ΔH_i is the enthalpy of adsorption.

For simplification of the system, some assumptions were considered as below:

1. One dimensional model with pseudo-homogenous packed bed reactor was considered
2. Isothermal and isobaric conditions were assumed because there was no detection of pressure and temperature drop since they were accurately controlled throughout the reaction.
3. No deactivation was recorded after 60 h on the stream; hence system was in steady-state
4. Due to high gas flow rate and low reactor diameter, radial and axial dispersion can be neglected

Then, the steady state design equation below (eq. 13) for packed bed reactor was used for estimation of kinetic parameters:

$$\frac{dy_i}{dw} = \frac{\sum_i^n v_i r_j}{F} \quad (6)$$

Where y_i is molar fraction of compound i , w is catalyst weight, v_i is the stoichiometric coefficient of each compound in the reaction rate r_j of reaction j and F is the molar flowrate.

For parameter estimation, MATLAB R2022a software was used to solve the system of differential equations using Runge-Kutta method of order 4-5 with k_j^0 , Ea_j , K_i^0 , ΔH_i being parameters to be optimized. For optimization, objective function was minimization of sum of square errors (SSE) between experimental and simulated molar fraction values of components defined as:

$$SSE = \sum_{n=1}^{n_e} (y_i^{sim} - y_i^{exp})_n^2 \quad (7)$$

Where w_i is the weight factor for each compound, y_i^{sim} and y_i^{exp} are calculated and experimental molar fractions, n_c and n_e are number of compounds and experiments respectively. The MATLAB function of *nlpaci* was used to determine 95% confidence intervals where *Jacobian* matrix is obtained from *lsqcurvefit* optimization function.

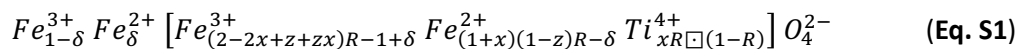
1.2 Process simulation

The reactor simulation was modelled in Aspen Plus V12 software under steady-state conditions. The PR-BM property method was used that is based on Peng-Robinson equation of state with Boston-Mathias modifications. To use the estimated kinetic parameters in reactor simulation, they were reparametrized in software's input conditions and units.

1.3 Formula determination of the catalyst

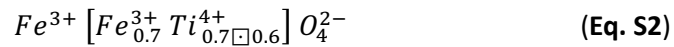
To determine the expected formula of the titanomaghemitic catalyst, the following considerations must be taken into account:

Titanomaghemites are metastable spinel-type mixed oxides with the general formula¹:



Where δ represents the number of Fe^{2+} ions, x is the variable related to Fe/Ti ratio ($Fe/Ti = \frac{3-x}{x}$), z is the fraction of Fe^{3+} in the spinel, and R is the spinel stoichiometry

parameter ($R = 8/[8 + z(1 + x)]$). Based on ICP elemental analysis, we determined $x = 0.909$. Additionally, XPS analysis showed no presence of Fe^{2+} , indicating $\delta = 0$ and $z = 1$. Therefore, the expected structural formula for FeTi@C550-5 is derived as:



2. Supplementary Figures

2.1 Characterization of MIL-88B (Fe, Ti)

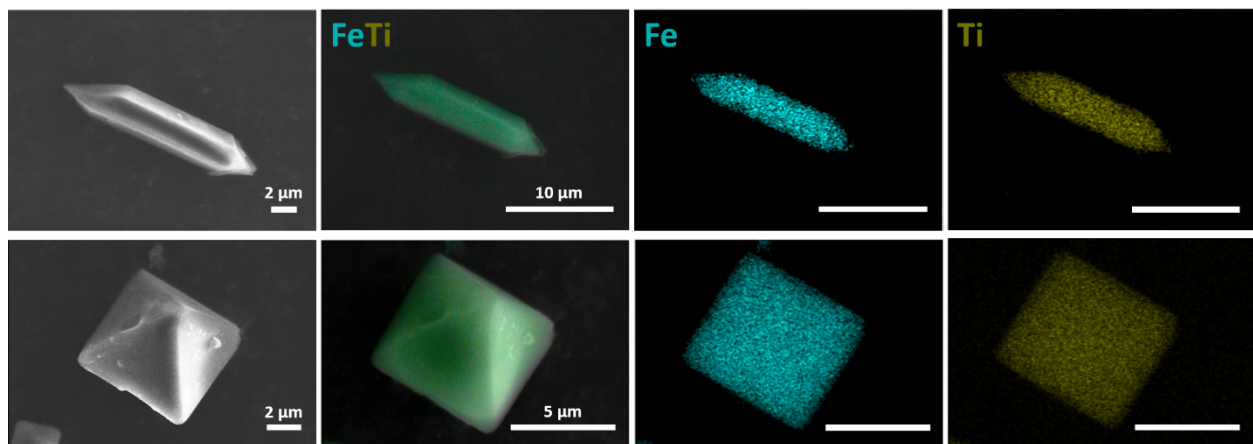


Figure S 1. SEM images and EDS mapping showing the distribution of Fe and Ti through-out the rod, and spindle-shaped MIL-88B (Fe,Ti) crystals.

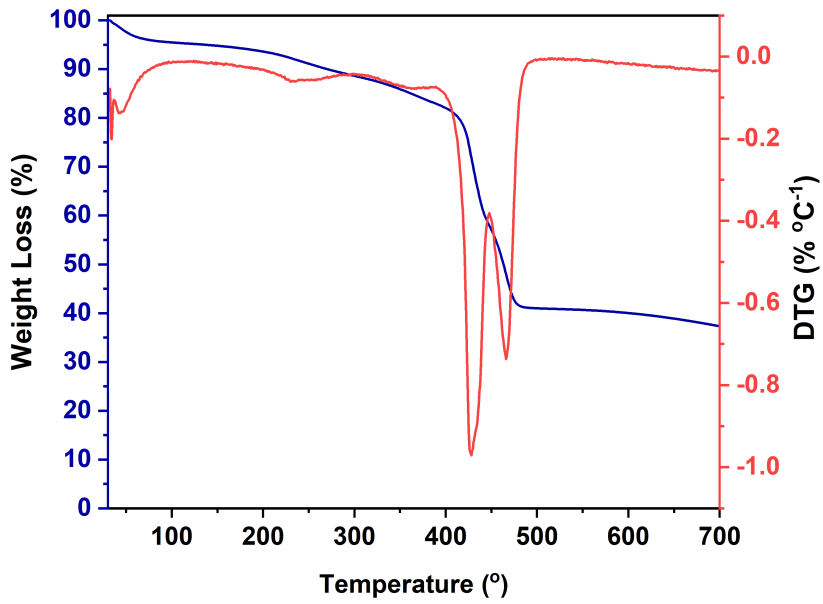


Figure S 2. TGA and DTG curves of **MIL-88B (Fe,Ti)**. Total weight loss ≈60%

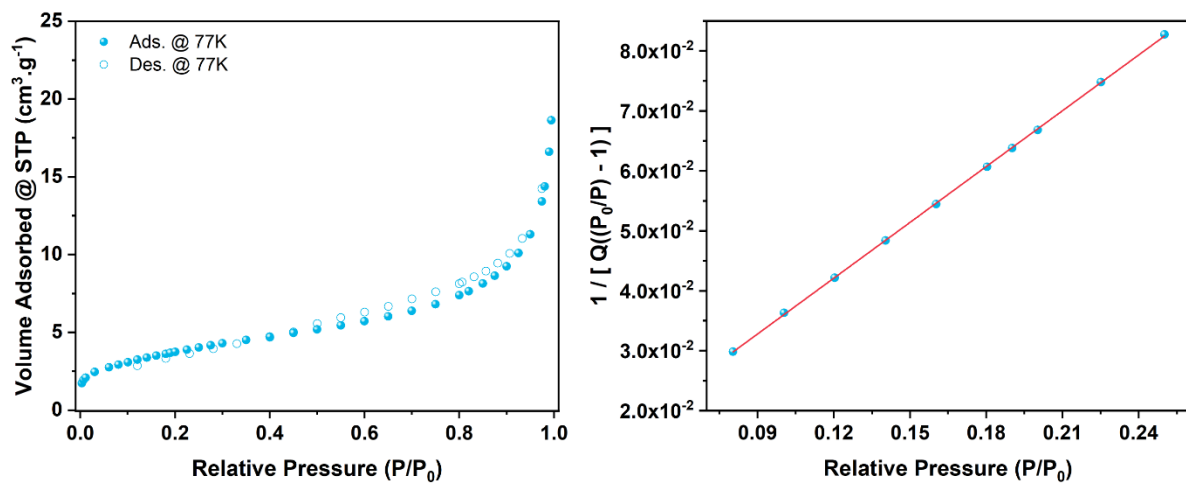


Figure S 3. N₂ adsorption isotherm at 77 K, and BET fit for **MIL-88B (Fe,Ti)**. BET surface area = 14 m²·g⁻¹.

2.2 Characterization of FeTi@C materials

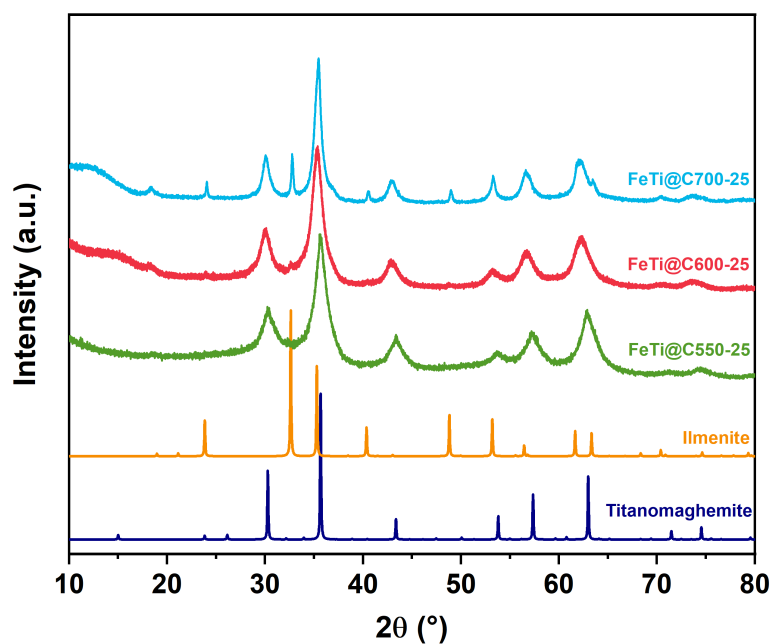


Figure S 4. PXRD patterns of FeTi@C550-25, FeTi@C600-25 and FeTi@C700-25 compared with the simulated PXRD patterns of titanomaghemite (dark blue), and ilmenite (orange).

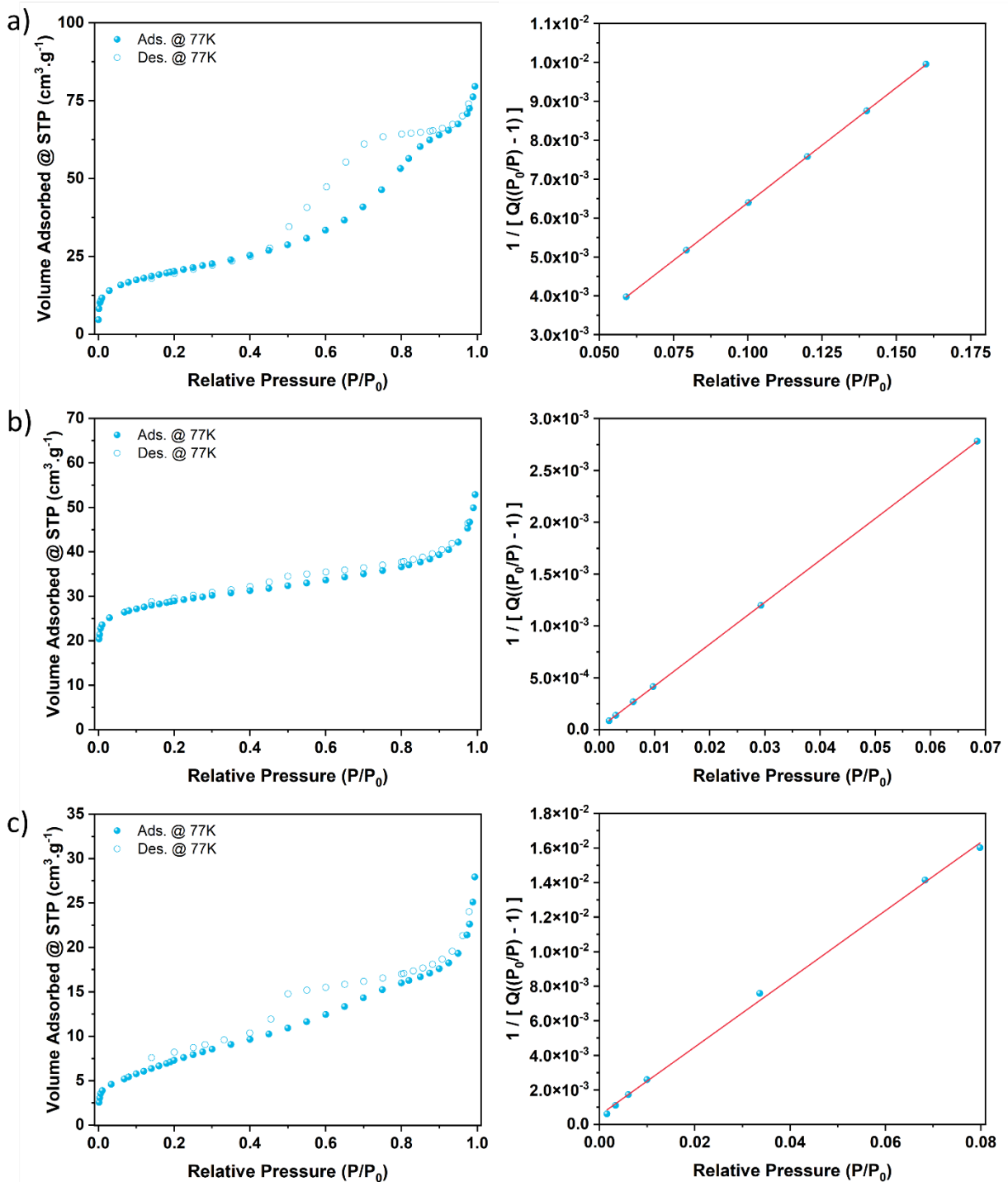


Figure S 5. N₂ Adsorption isotherms at 77 K and BET linear fit for a) FeTi@C550-25, b) FeTi@C600-25, and c) FeTi@C700-25.

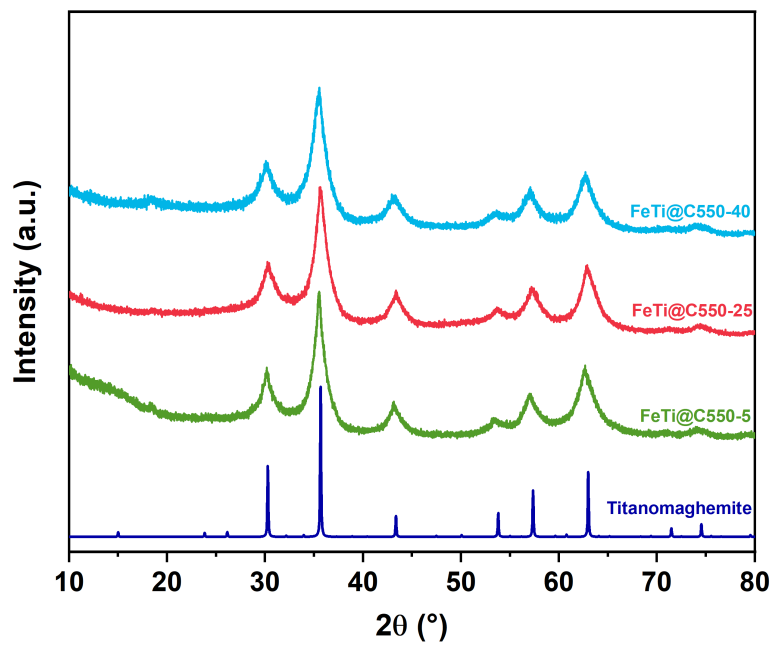


Figure S 6. PXRD patterns of FeTi@C550-5, FeTi@C550-25 and FeTi@C550-40 compared with the simulated PXRD pattern of titanomaghemite (dark blue).

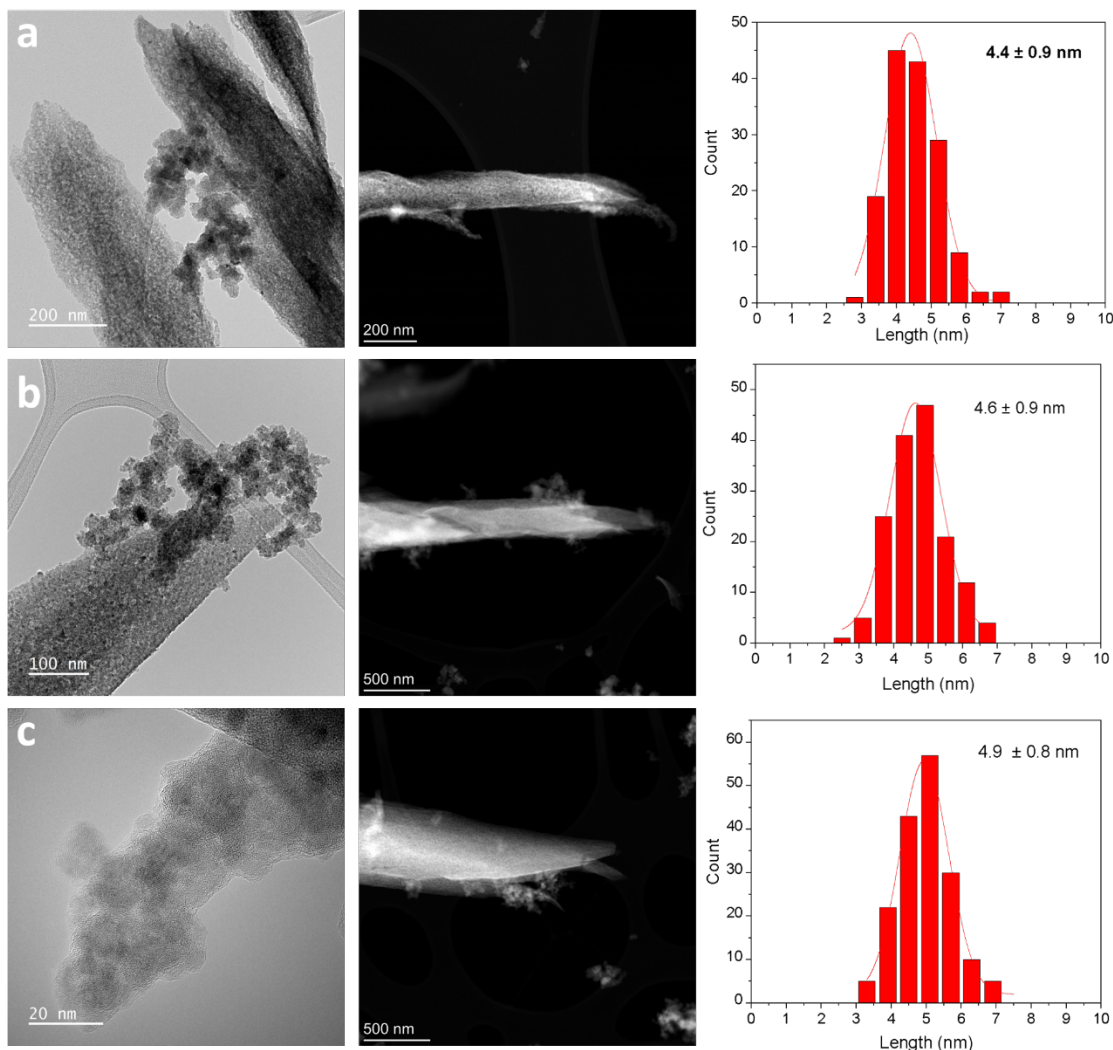


Figure S 7. TEM, HAADF-STEM and particle size distribution of a) FeTi@C550-5, b) FeTi@C550-25, and c) FeTi@C550-40.

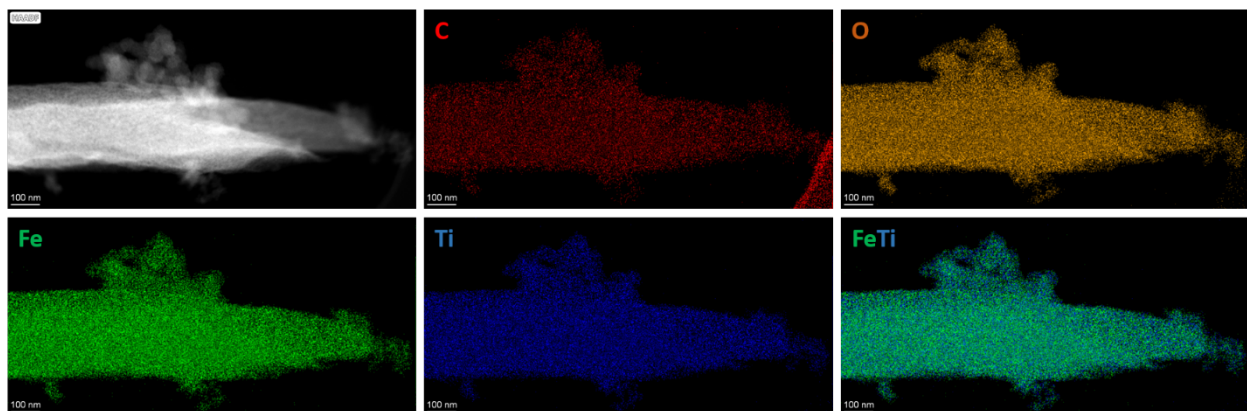


Figure S 8. Elemental mapping by STEM-EDX of an individual rod-shaped crystal of TiFe@C550-25 showing the homogeneous distribution of C (red), O (orange), Fe (green), and Ti (blue) throughout the solid.

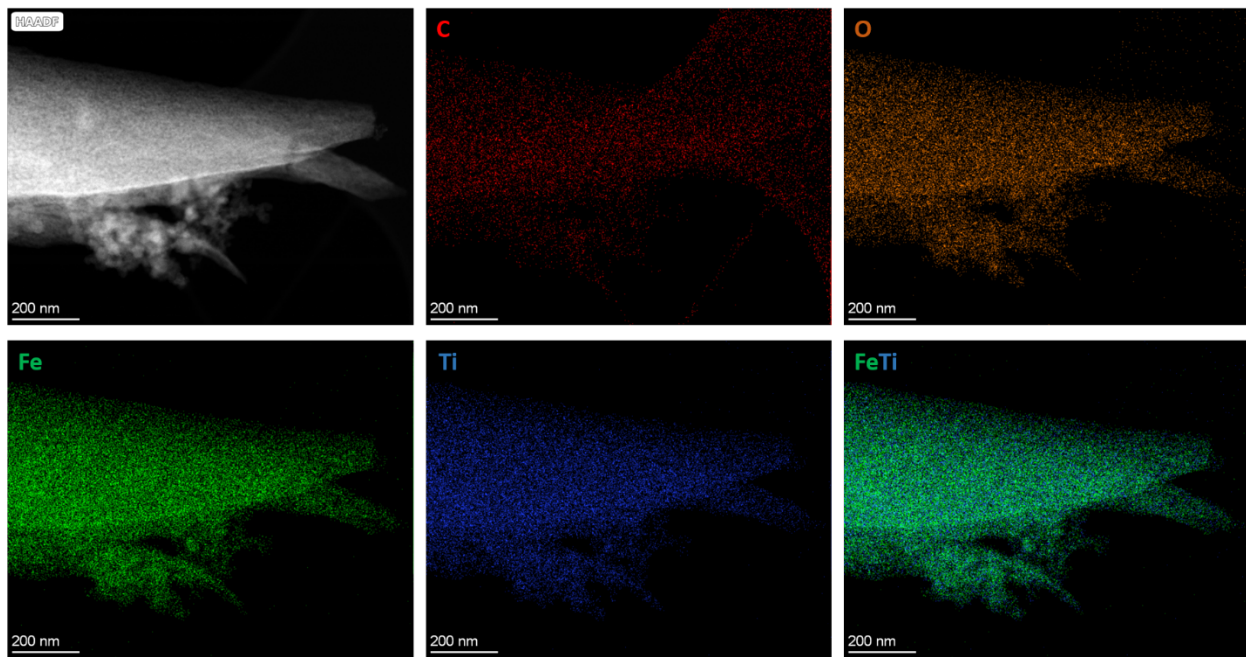


Figure S 9. Elemental mapping by STEM-EDX of an individual rod-shaped crystal of **TiFe@C550-40** showing the homogeneous distribution of C (red) O (orange), Fe (green), and Ti (blue) throughout the solid.

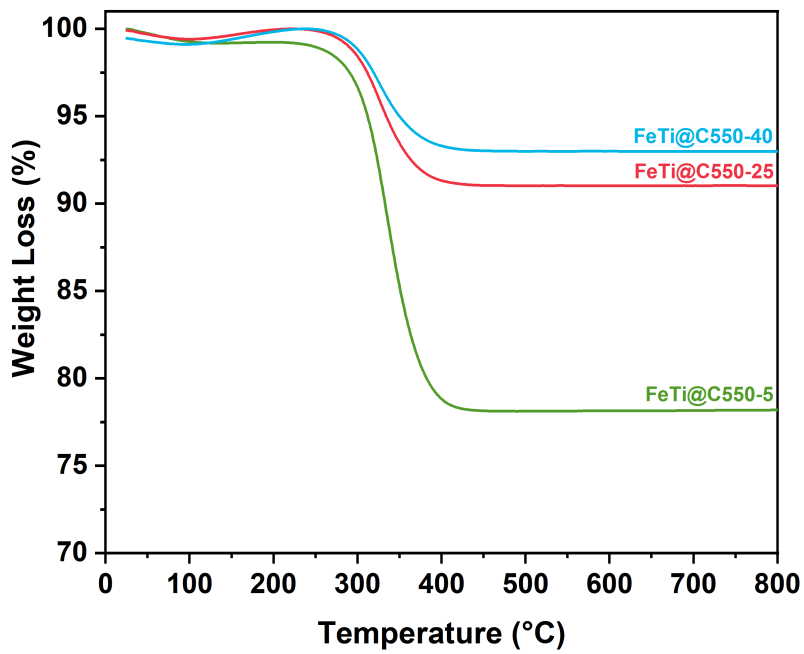


Figure S 10. TGA curves of **FeTi@C550-5**, **FeTi@C550-25**, and **FeTi@C550-40**.

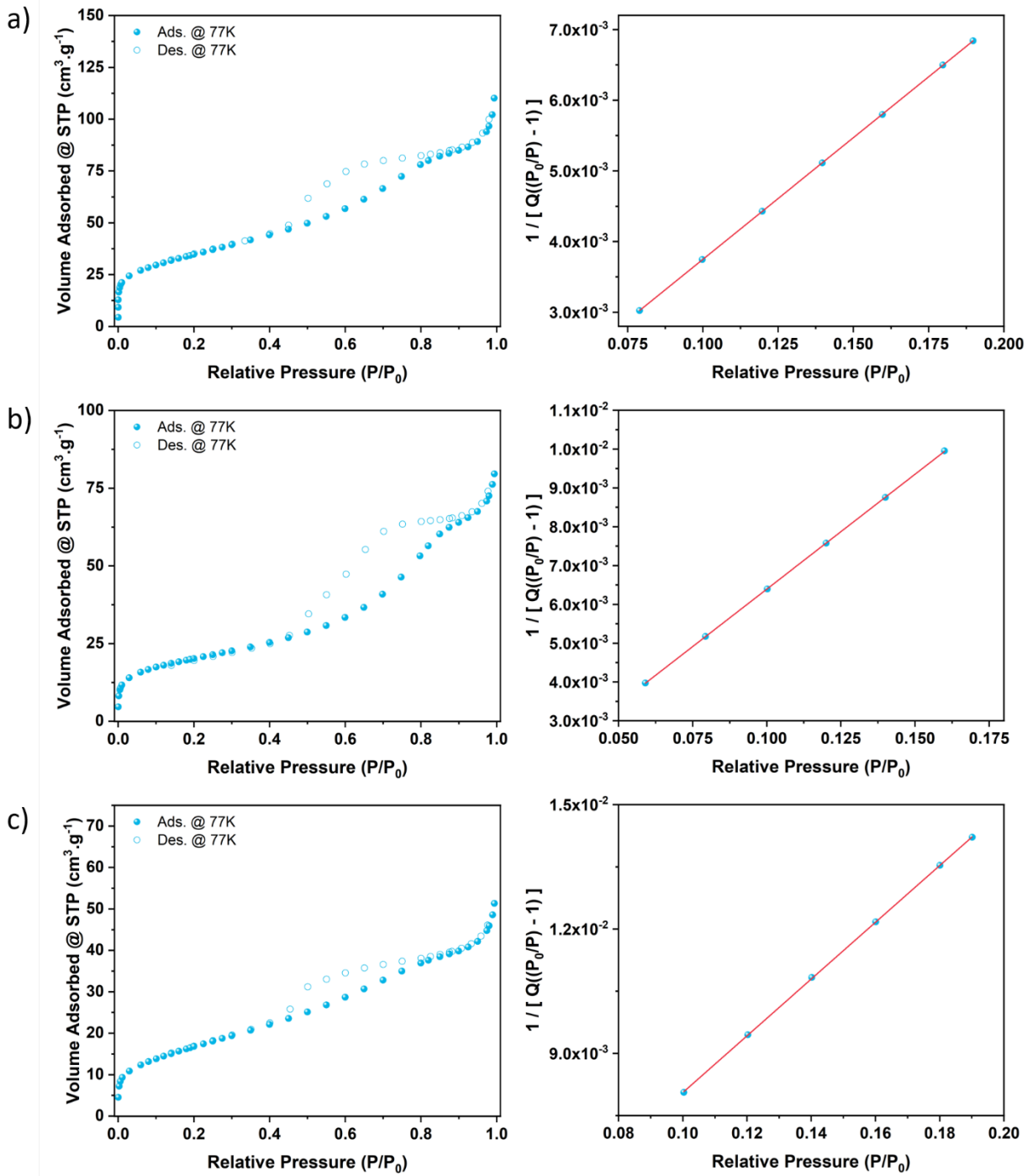


Figure S 11. N₂ Adsorption isotherms at 77 K and BET linear fit for a) FeTi@C550-5, b) FeTi@C550-25, and c) FeTi@C550-40.

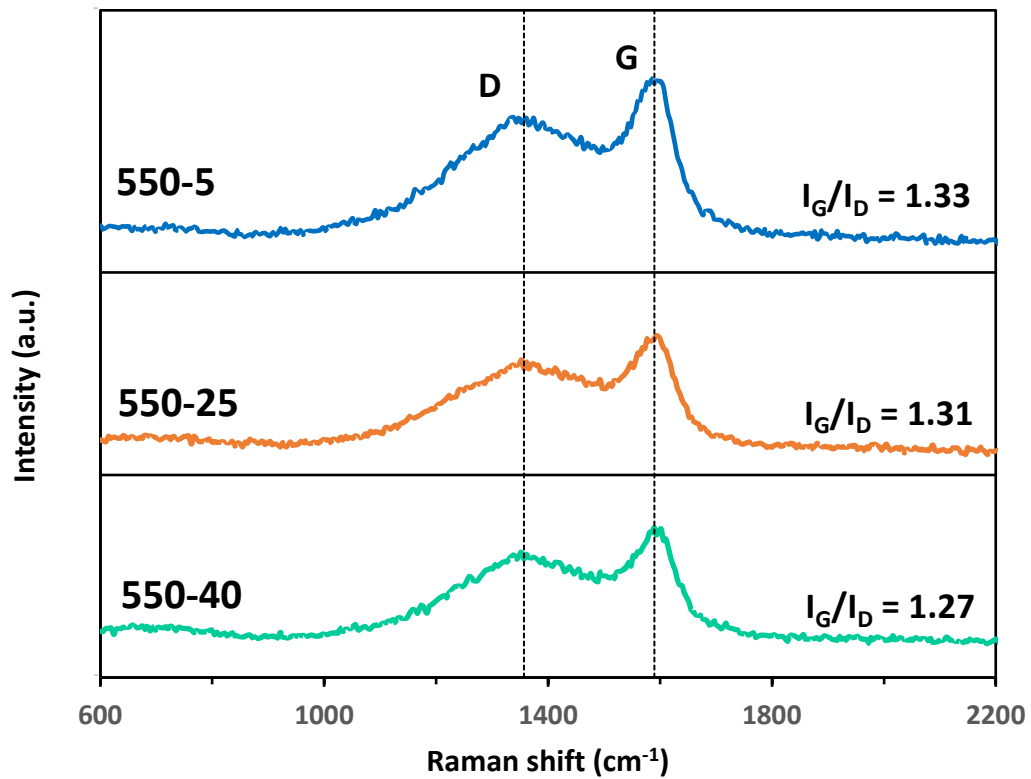


Figure S 12. Raman spectroscopy curves of FeTi@C550-X ($X = 5, 25, 40 \text{ }^{\circ}\text{C}$).

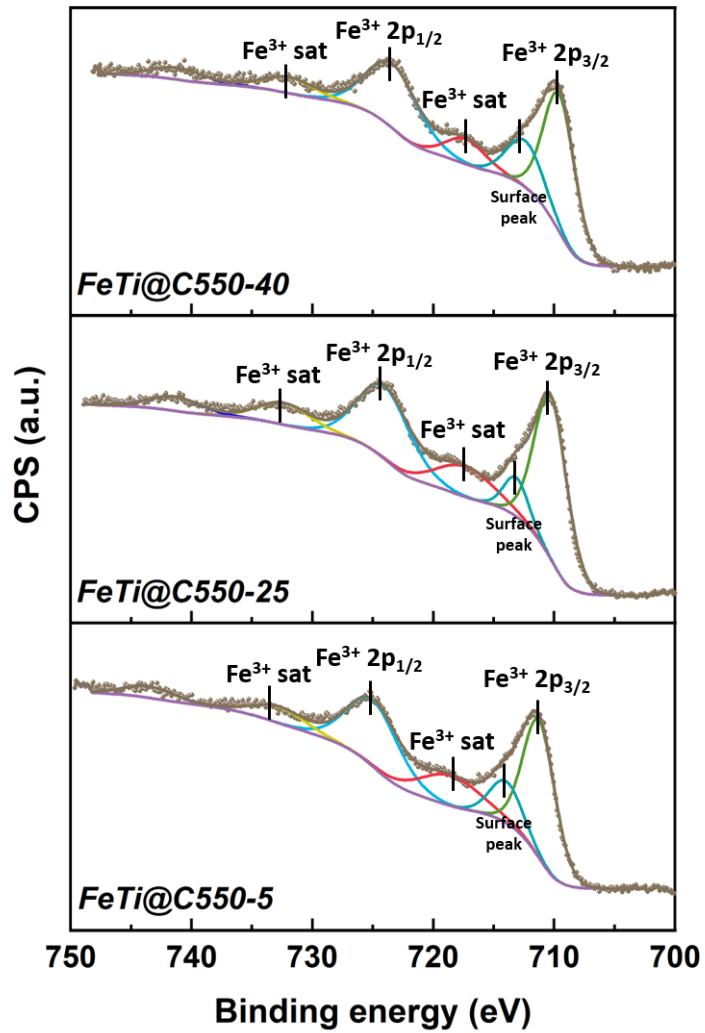


Figure S 13. X-ray photoelectron spectroscopy of the **FeTi@C550-X** catalyst with core level Fe(2p). The symbols are the experimental data, while the full lines are the components used for the decomposition of the spectra.

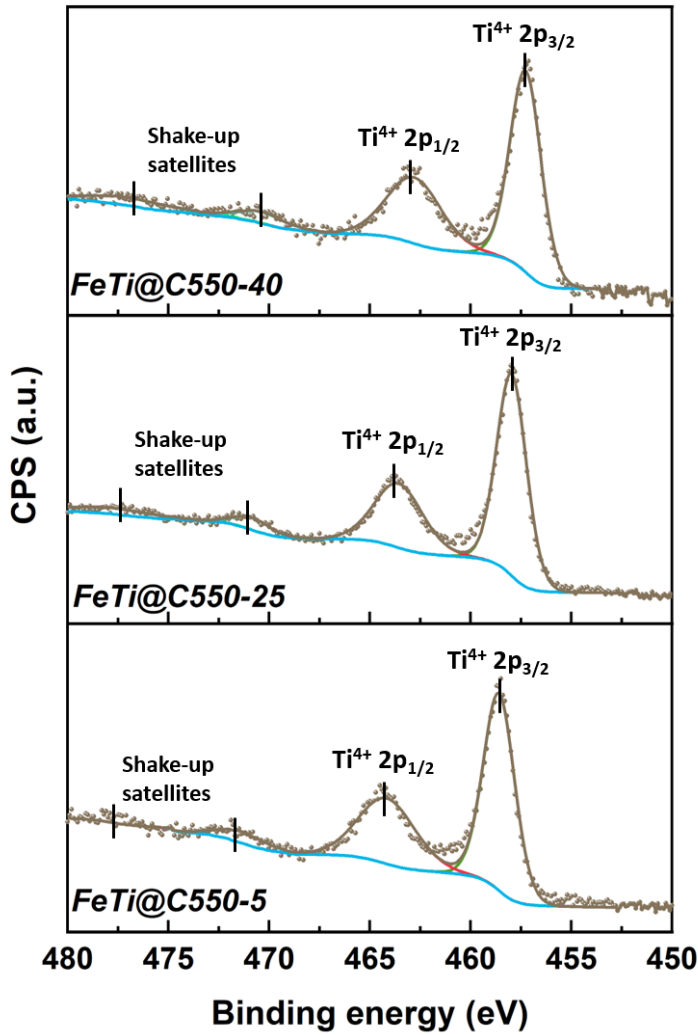


Figure S 14. X-ray photoelectron spectroscopy of the **FeTi@C550-X** catalyst with core level Ti(2p). The symbols are the experimental data, while the full lines are the components used for the decomposition of the spectra.

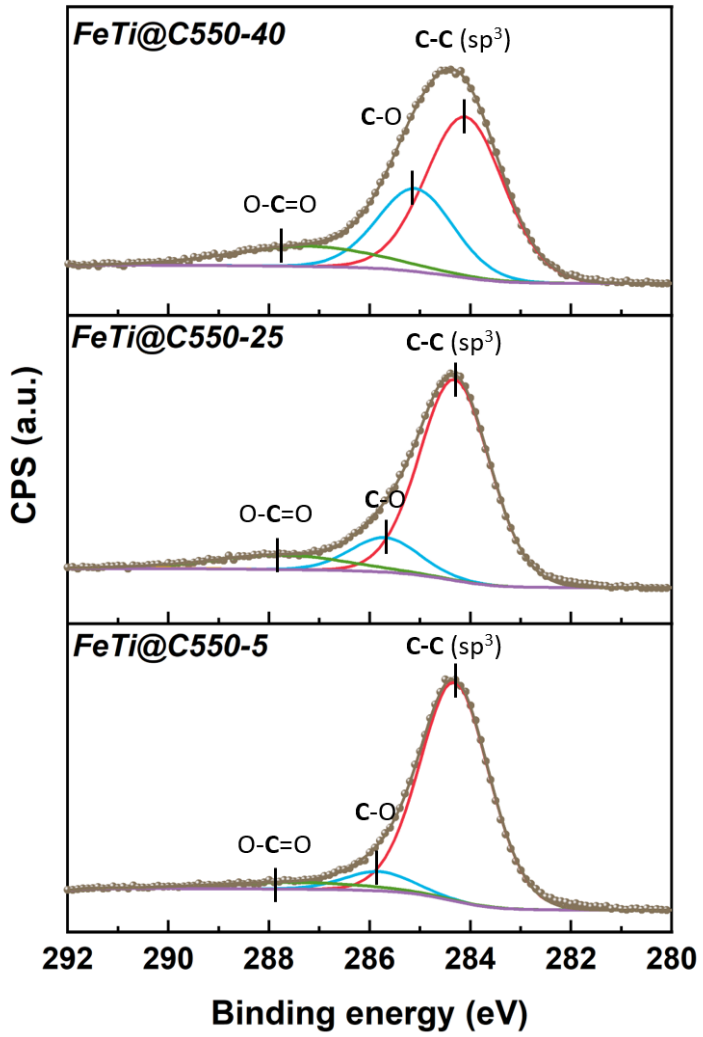


Figure S 15. X-ray photoelectron spectroscopy of the **FeTi@C550-X** catalyst with core level C(1S). The symbols are the experimental data, while the full lines are the components used for the decomposition of the spectra.

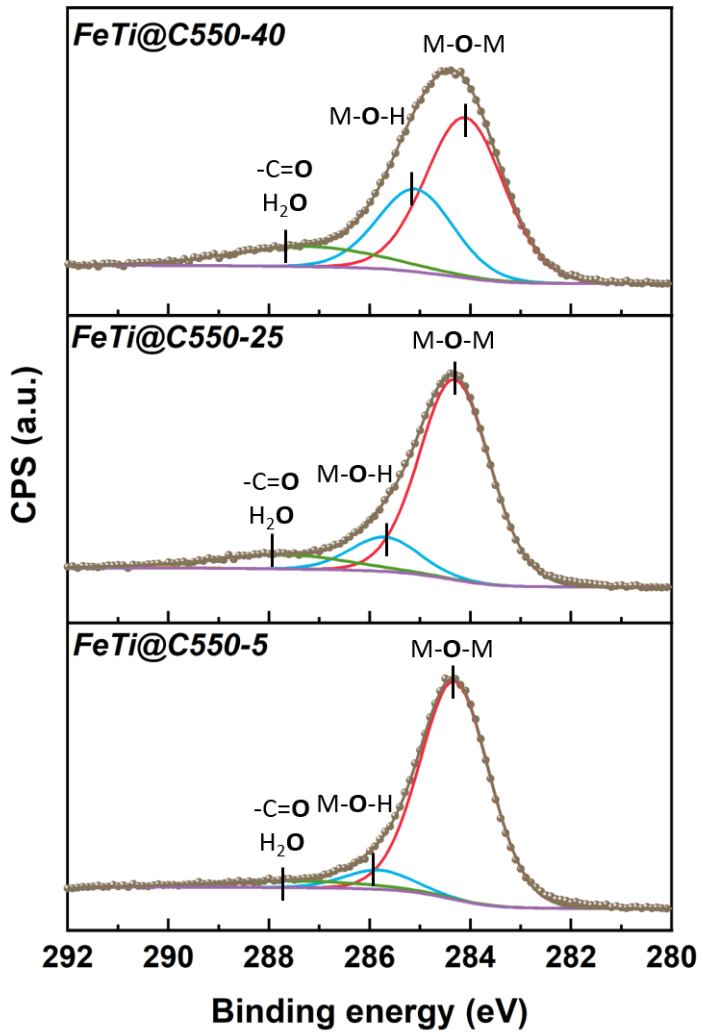


Figure S 16. X-ray photoelectron spectroscopy of the **FeTi@C550-X** catalyst with core level O(1S). The symbols are the experimental data, while the full lines are the components used for the decomposition of the spectra.

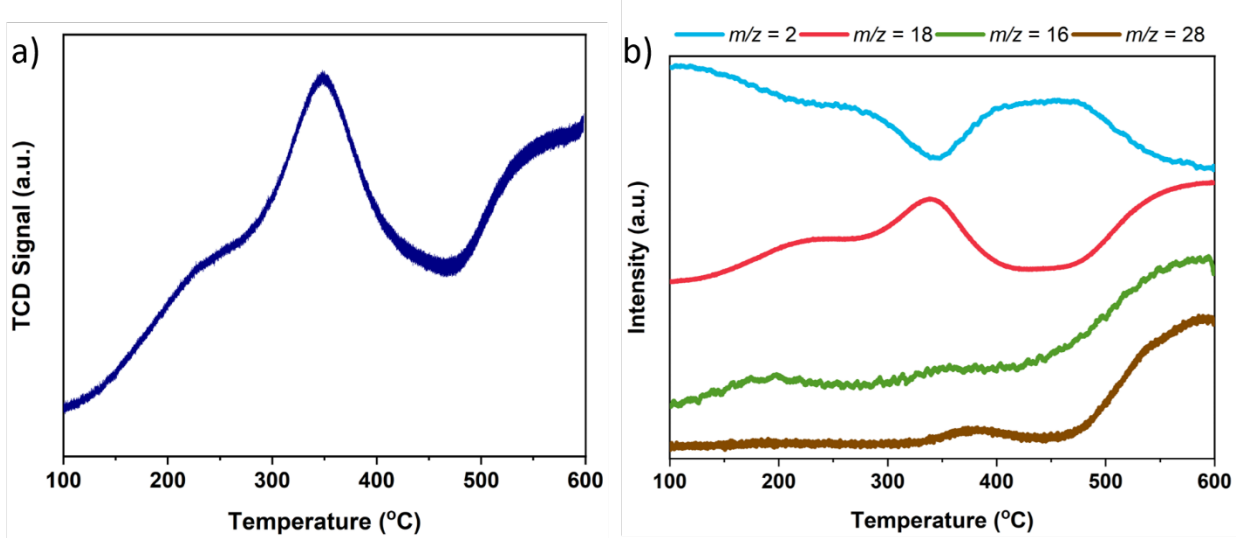


Figure S 17. Temperature-programmed reduction (H₂-TPR) profile of the FeTi@C550-5 recorded by mass spectrometry.

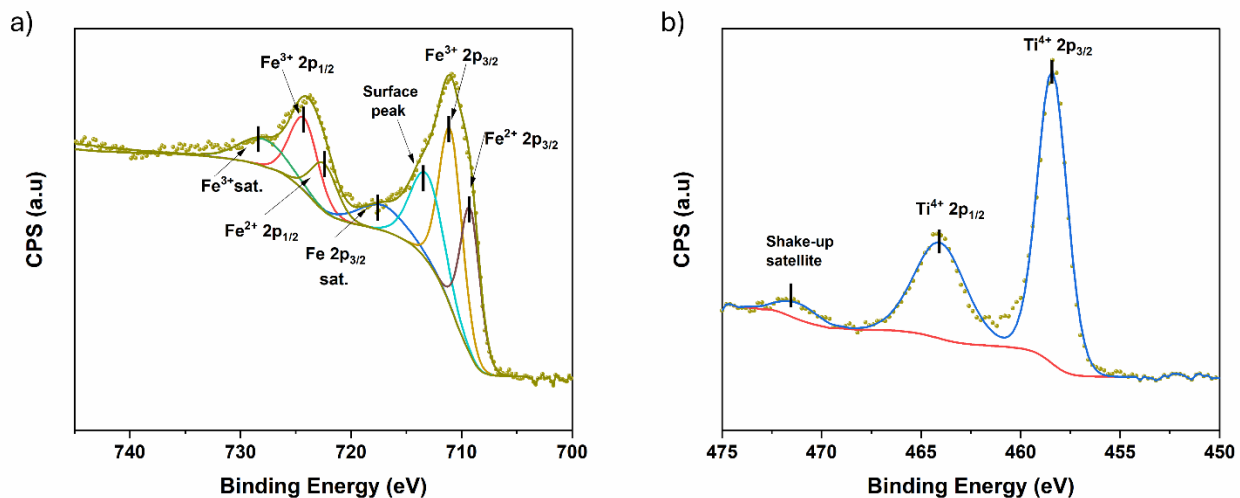


Figure S 18. X-ray photoelectron spectroscopy of the in-situ reduced FeTi@C550-X catalyst with core level Fe(2p). The symbols are the experimental data, while the full lines are the components used for the decomposition of the spectra

2.3 Characterization of Spent Catalysts

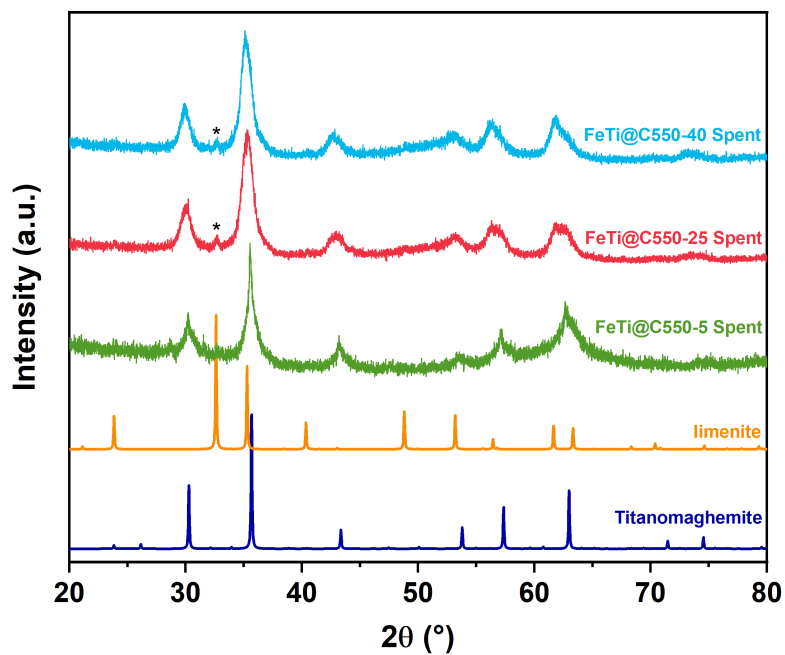


Figure S 19. PXRD patterns of FeTi@C550-5, FeTi@C550-25 and FeTi@C550-40 after reaction compared with the simulated PXRD patterns of titanomaghemite (dark blue), and ilmenite (orange).

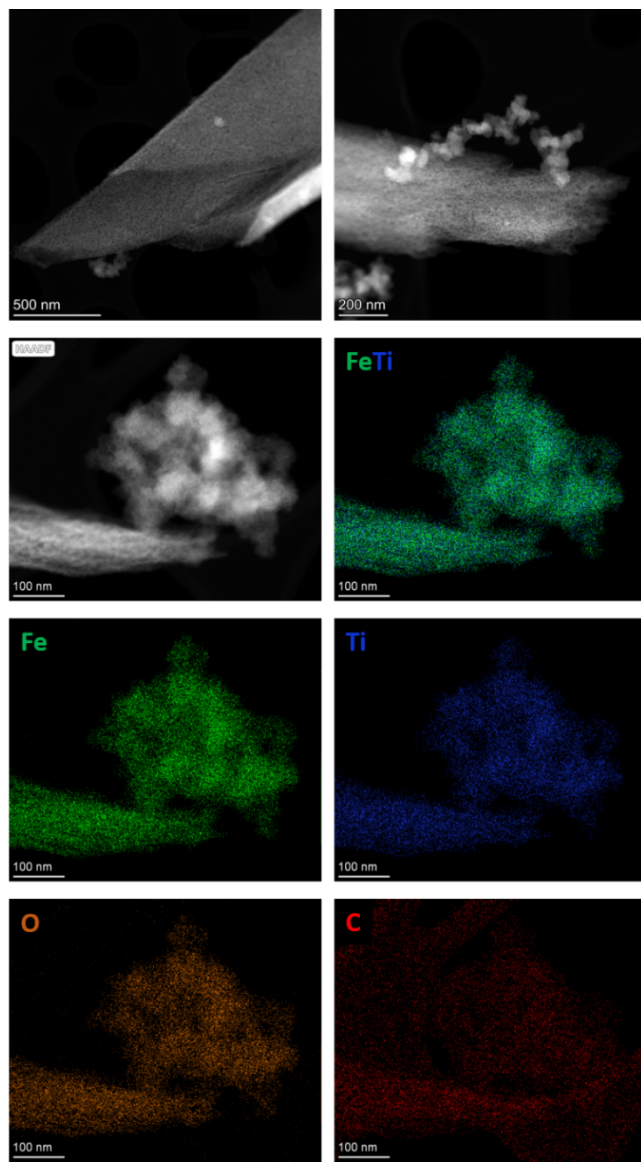


Figure S 20. HAADF-STEM and Elemental mapping by STEM-EDX of spent FeTi@C550-5 catalyst.

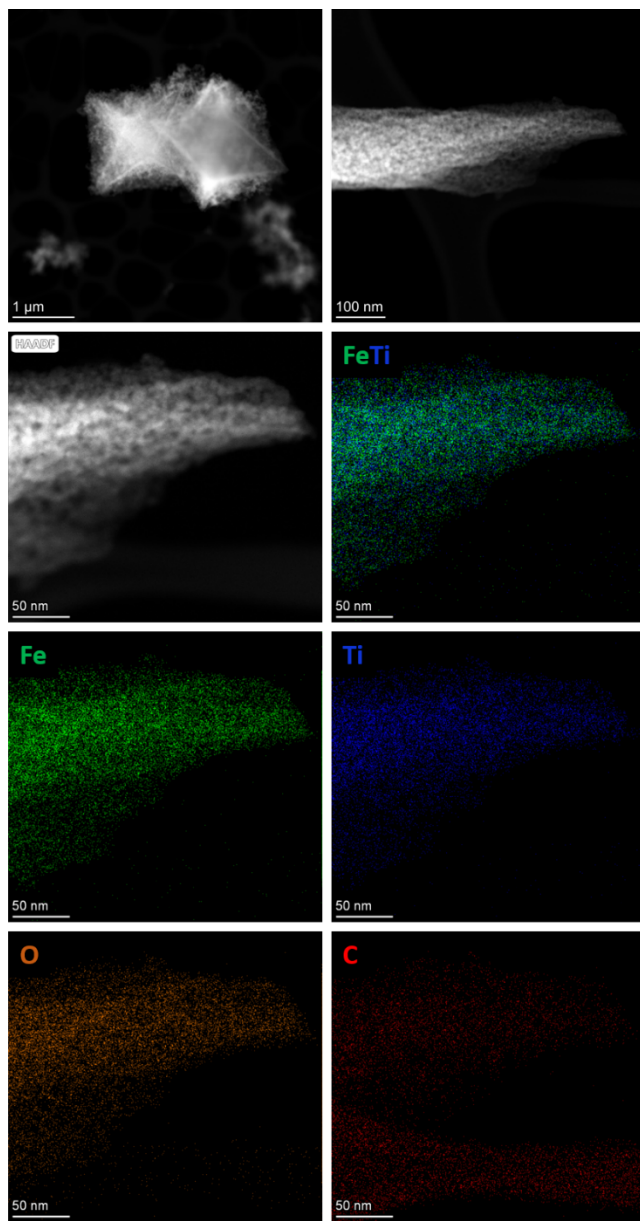


Figure S 21. HAADF-STEM and Elemental mapping by STEM-EDX of spent **FeTi@C550-25** catalyst.

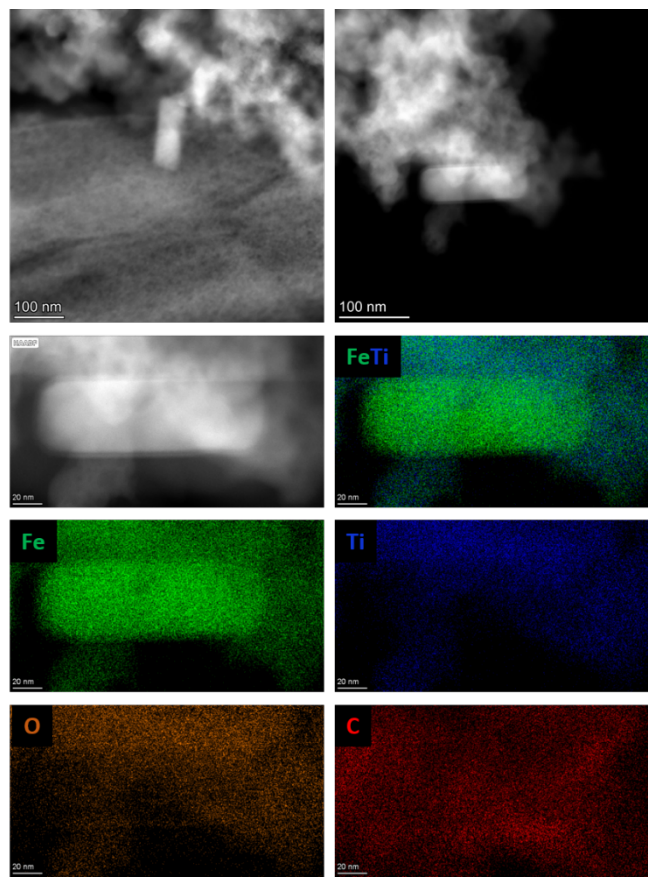


Figure S 22. HAADF-STEM and Elemental mapping by STEM-EDX of spent **FeTi@C550-40** catalyst.

2.4 Catalytic Results

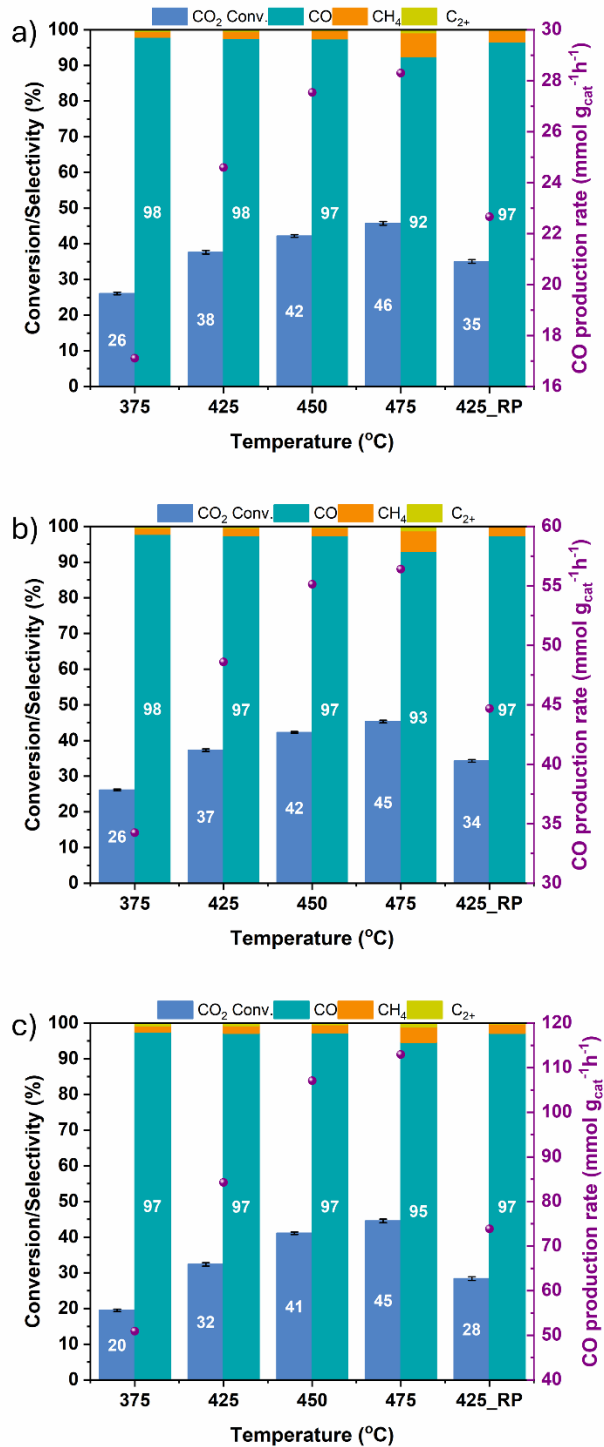


Figure S 23. Temperature optimization results for the catalytic CO_2 reduction over **FeTi@C550-5**. 425_RP refers to return point to 425 °C after catalytic analysis at 375-475 °C. Reaction conditions: $\text{H}_2/\text{CO}_2 = 3$, $P = 30$ bar, GHSV = a) 6000 $\text{mL}\cdot\text{g}^{-1}\cdot\text{h}^{-1}$, b) 12000 $\text{mL}\cdot\text{g}^{-1}\cdot\text{h}^{-1}$, and c) 24000 $\text{mL}\cdot\text{g}^{-1}\cdot\text{h}^{-1}$.

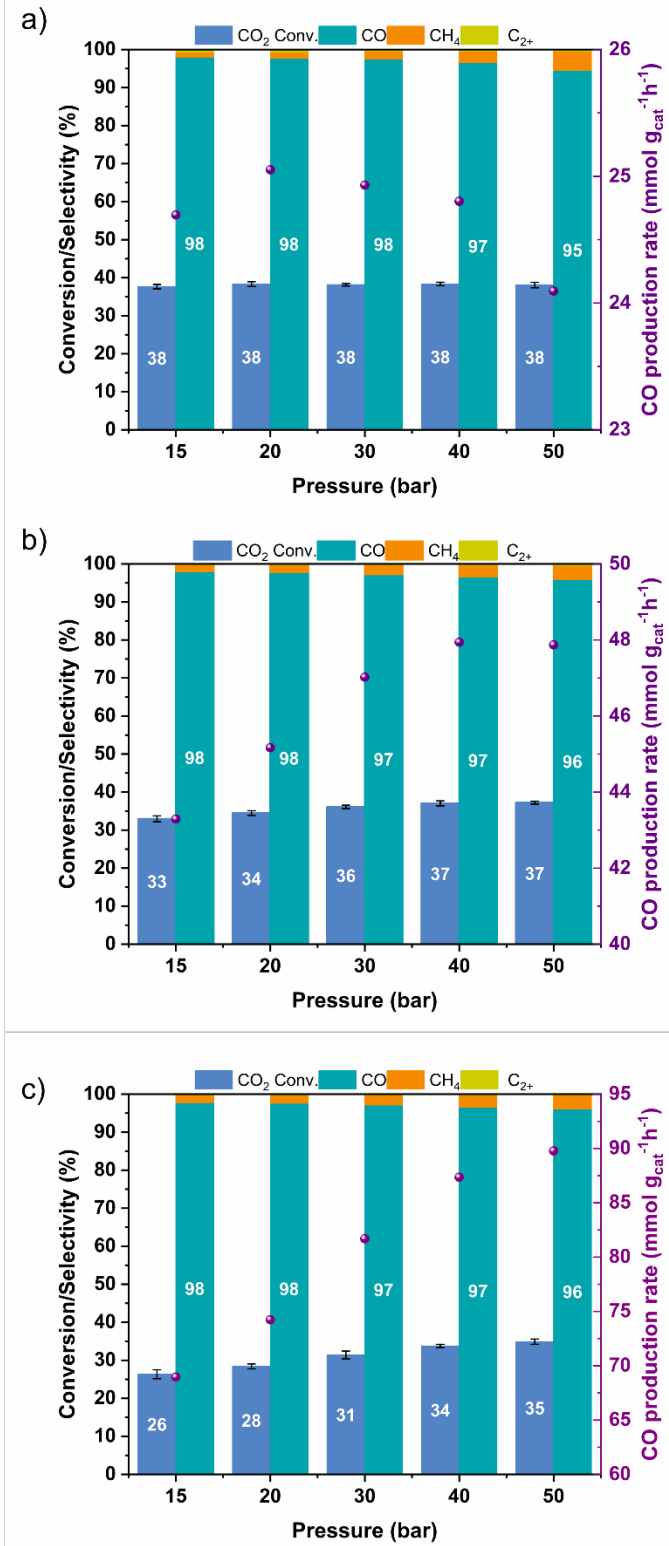


Figure S 24. Pressure optimization results for the catalytic CO₂ reduction over **FeTi@C550-5**. Reaction conditions: H₂/CO₂ = 3, T = 425 °C, and GHSV = a) 6000 mL·g⁻¹·h⁻¹, b) 12000 mL·g⁻¹·h⁻¹, and c) 24000 mL·g⁻¹·h⁻¹.

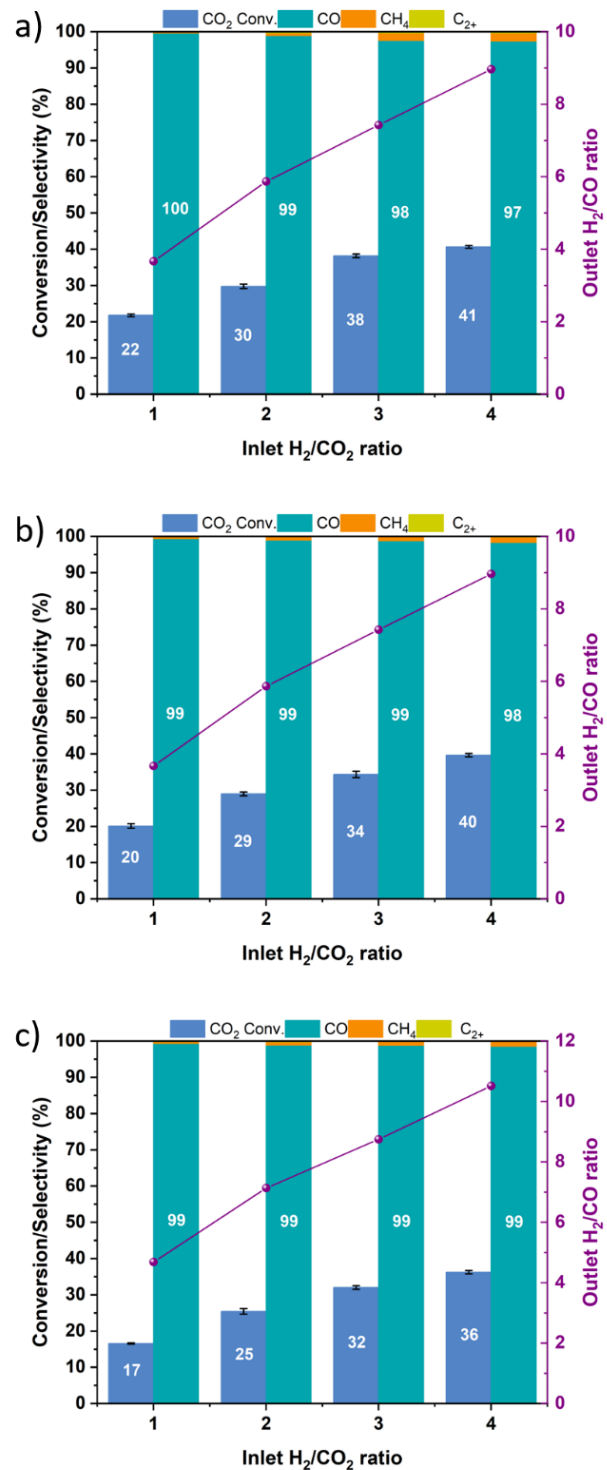


Figure S 25. Feed ratio optimization results for the catalytic CO₂ reduction over **FeTi@C550-5**. Reaction conditions: P = 20 bar, T = 425 °C, and GHSV = a) 6000 mL·g⁻¹·h⁻¹, b) 12000 mL·g⁻¹·h⁻¹, and c) 24000 mL·g⁻¹·h⁻¹.

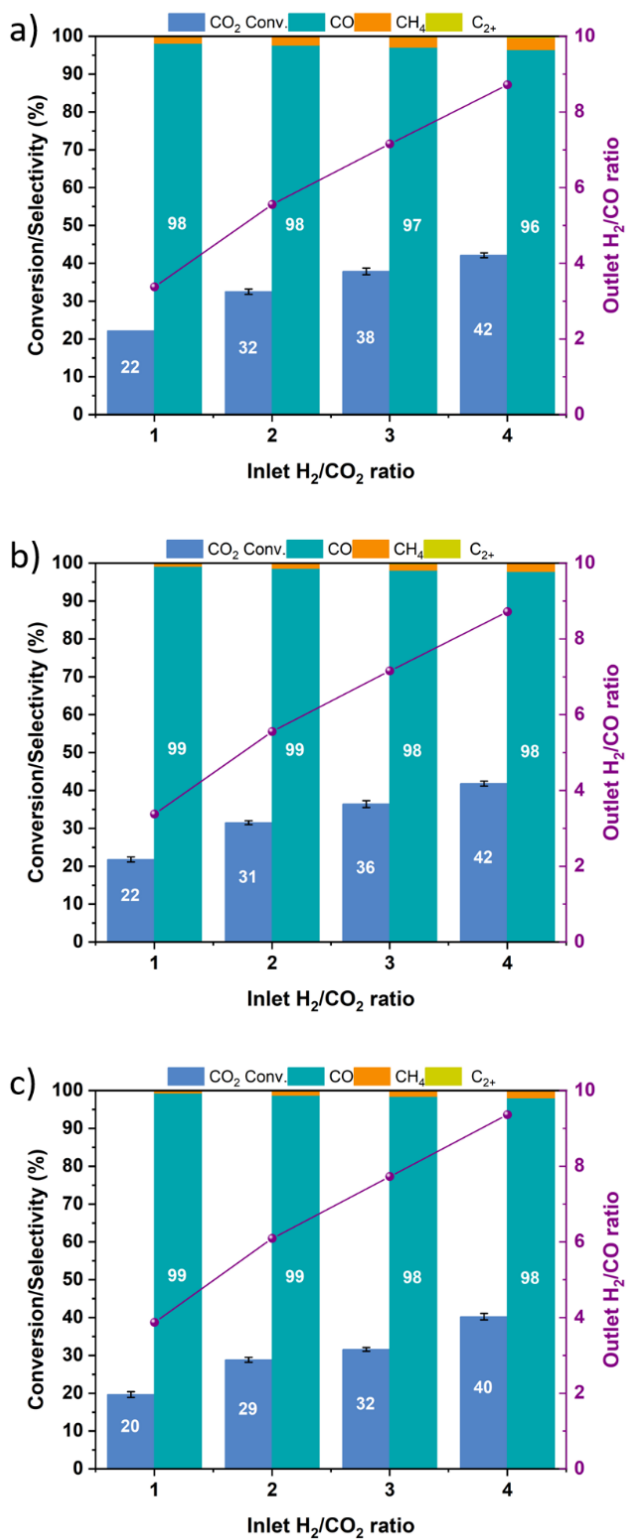


Figure S 26. Feed ratio optimization results for the catalytic CO₂ reduction over **FeTi@C550-5**. Reaction conditions: P = 30 bar, T = 425 °C, and GHSV = a) 6000 mL·g⁻¹·h⁻¹, b) 12000 mL·g⁻¹·h⁻¹, and c) 24000 mL·g⁻¹·h⁻¹.

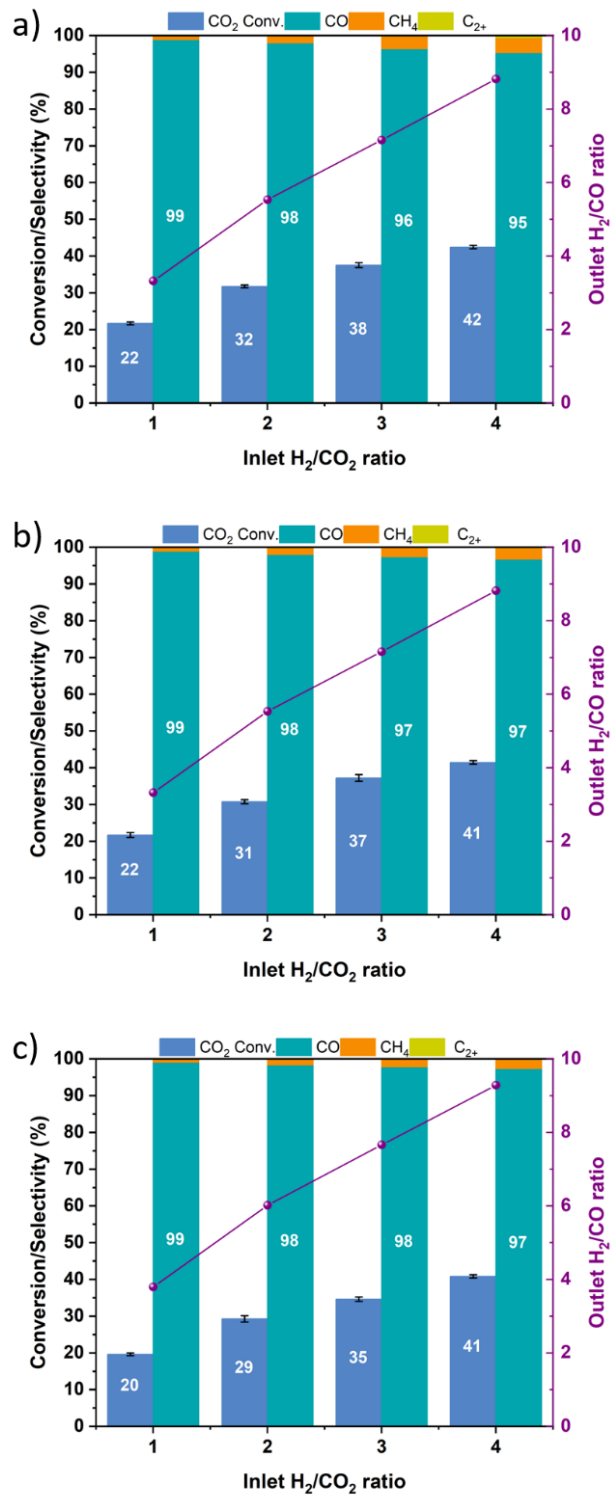


Figure S 27. Feed ratio optimization results for the catalytic CO_2 reduction over **FeTi@C550-5**. Reaction conditions: $P = 40$ bar, $T = 425^\circ\text{C}$, and GHSV = a) $6000 \text{ mL}\cdot\text{g}^{-1}\cdot\text{h}^{-1}$, b) $12000 \text{ mL}\cdot\text{g}^{-1}\cdot\text{h}^{-1}$, and c) $24000 \text{ mL}\cdot\text{g}^{-1}\cdot\text{h}^{-1}$.

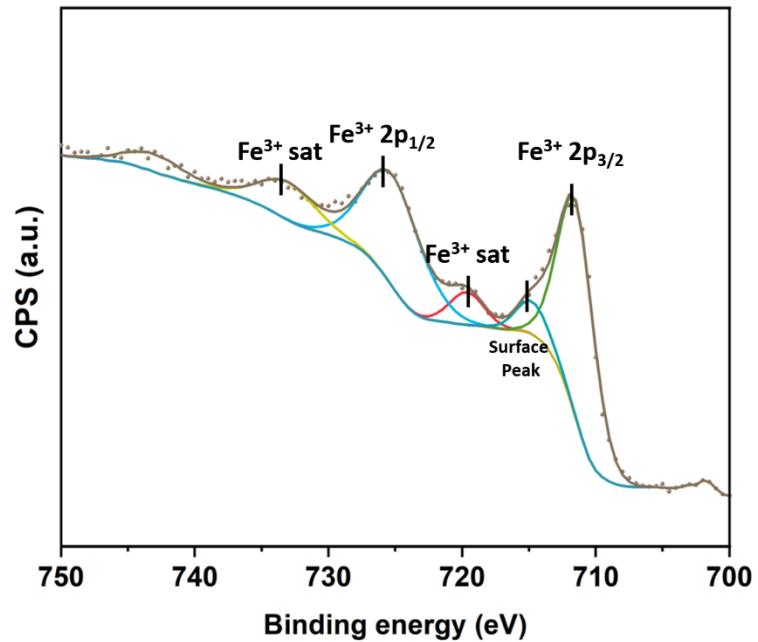


Figure S 28. X-ray photoelectron spectroscopy of the **FeTi@C550-5** catalyst after 60h of reaction with core level Fe(2p). The symbols are the experimental data, while the full lines are the components used for the decomposition of the spectra.

2.5 Kinetic Study Results

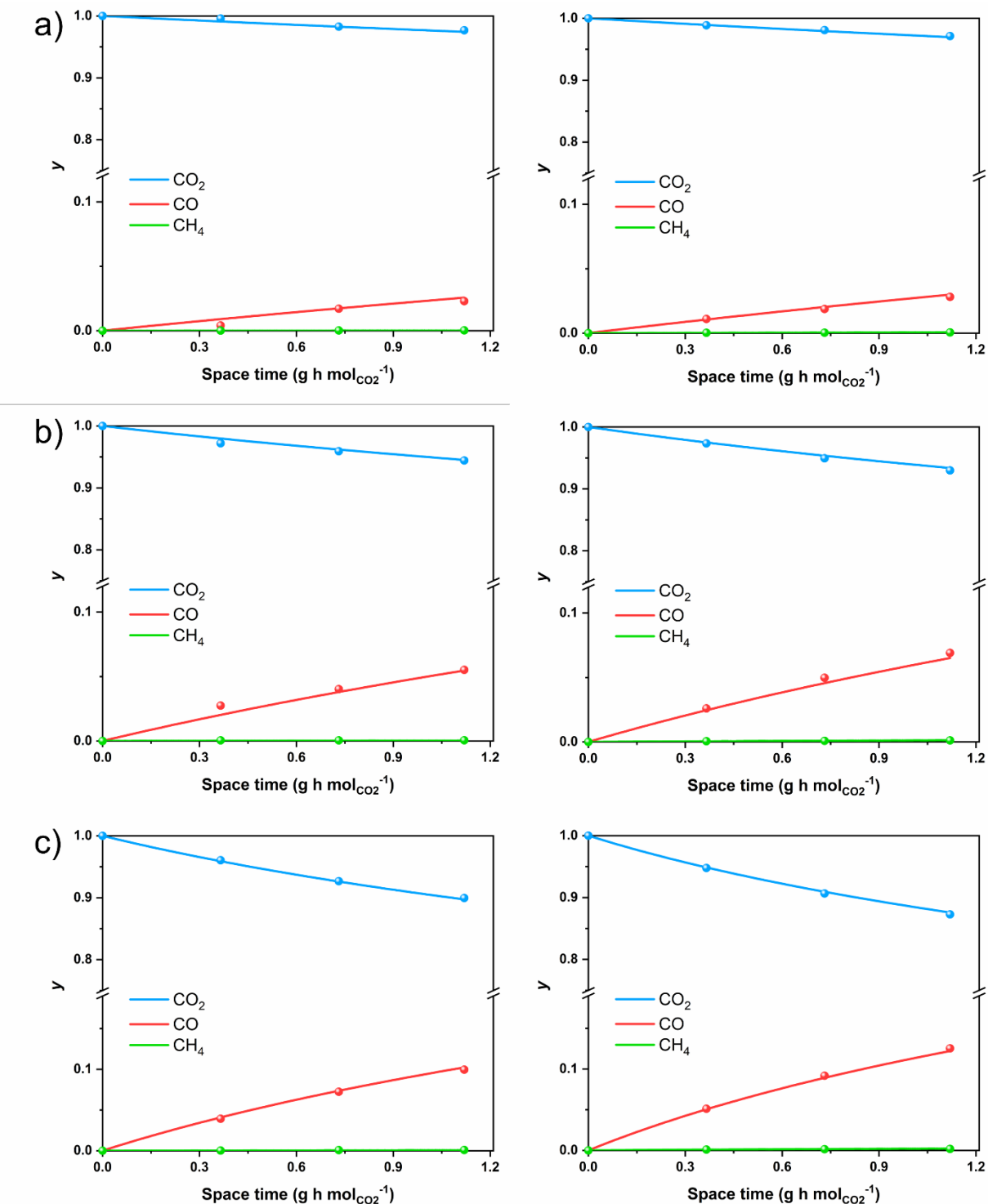


Figure S 29. Experimental data fitting of CO_2 hydrogenation reaction over the **FeTi@C550-5** catalyst at 20 bar (left), 40 bar (right) and at a) 375 °C, b) 400 °C and c) 425 °C.

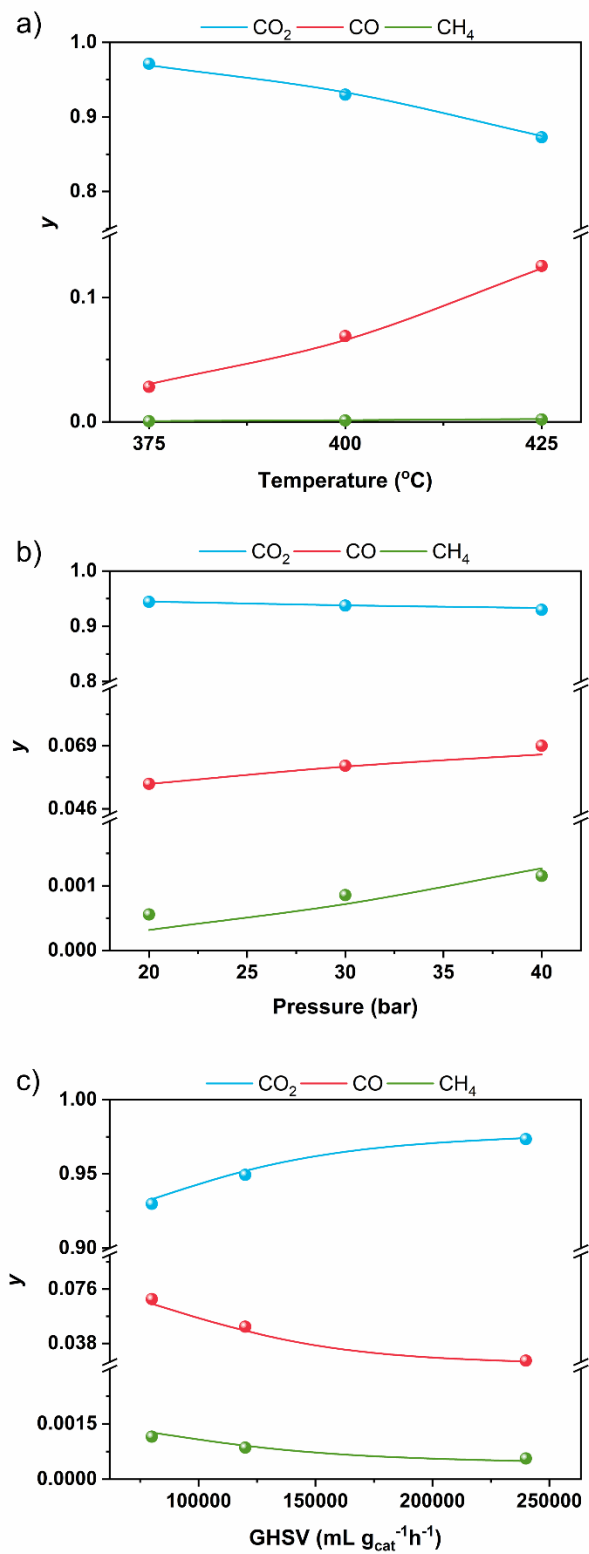


Figure S 30. Experimental data fitting of CO_2 hydrogenation reaction over the **FeTi@C550-5** catalyst at different reaction conditions.

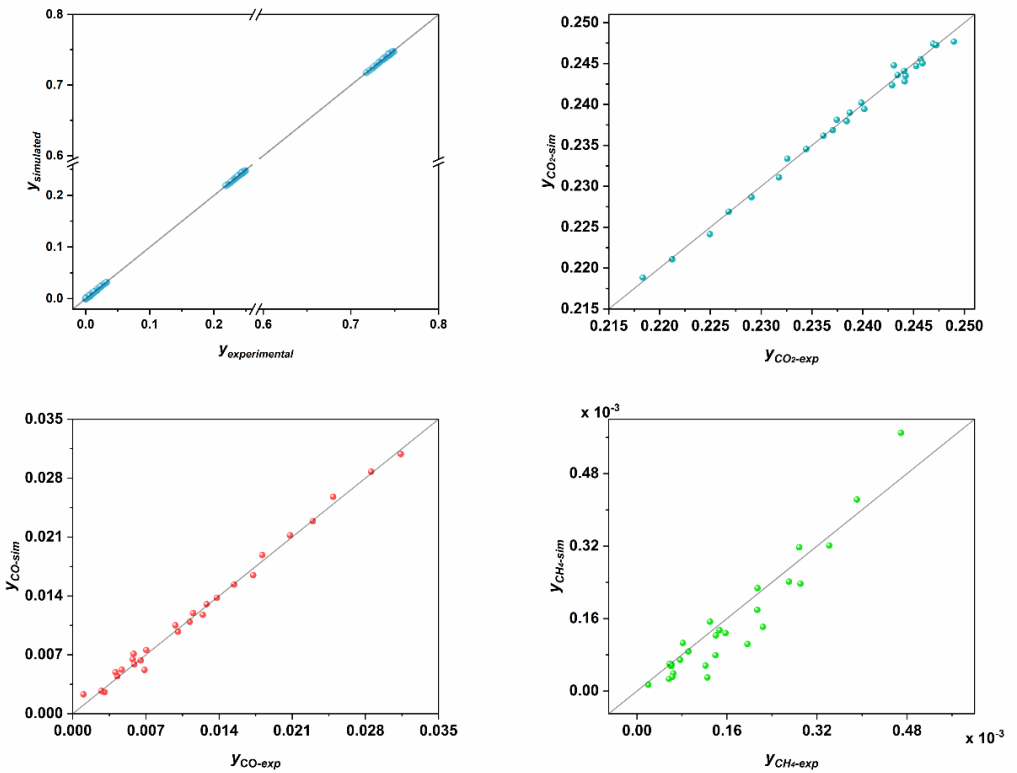


Figure S 31. Parity plot of the calculated and experimental molar fractions.

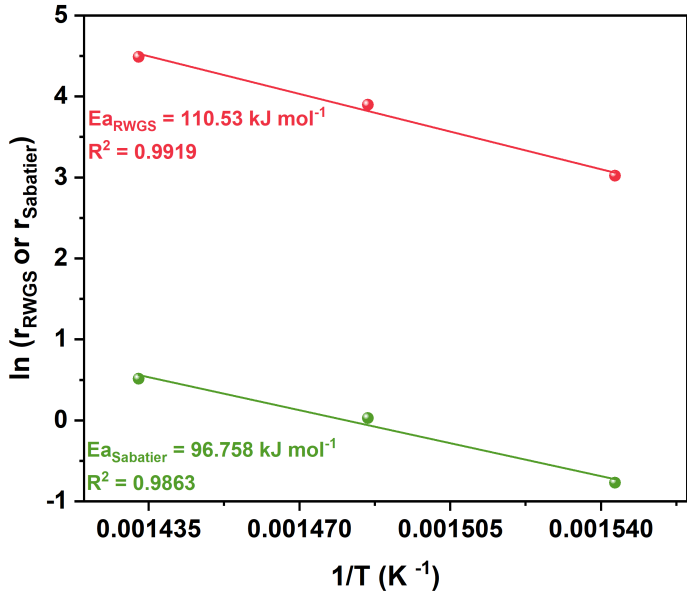


Figure S 32. Arrhenius plots for RWGS and Sabatier reactions.

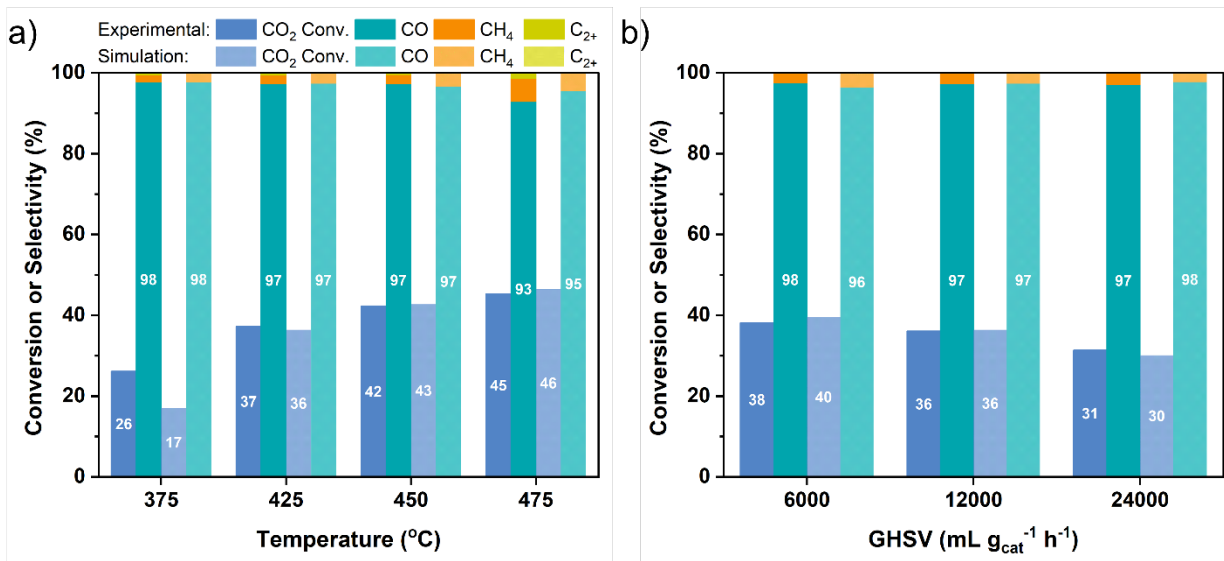


Figure S 33. Simulation results using the estimated kinetic parameters compared with experimental catalytic data on FeTi@C550-5 at different a) Temperature, and b) GHSV. Other reaction conditions: H₂/CO₂ = 3, T = 425 °C, P = 30 bar, GHSV = 12000 mL gcat⁻¹h⁻¹

3. Supplementary Tables

Table S 1. ICP-OES measurement results

Element	Fe (at%)	Ti (at%)	Fe/Ti ratio
FeTi@C550-5	34.4	14.8	2.3
FeTi@C550-25	42.1	17.7	2.3
FeTi@C550-40	49.1	20.7	2.3

Table S 2. Summary of state-of-art high-pressure RWGS catalysts

Catalyst	H ₂ /CO ₂	T (°C)	P (bar)	GHSV (mL·g ⁻¹ ·h ⁻¹ or h ⁻¹)	CO ₂ Conversion (%)	CO Selectivity (%)	Stability	Ref.
FeTi@C550-5	3	425	30	64000	22	98	60 h	This work
TiFe@C	3	425	30	24000	38.4	96.3	48 h	²
CuK/C	3	260	20	4000	17.5	100	85 h ^a	³
CuNa/C	3	260	20	4000	16.7	98.9		
Cu/C	3	260	20	4000	7.6	95.5		
K-Mo ₂ C/y-Al ₂ O ₃	3	450	20	132, 120	42.7	99.1	120 h	⁴
Ni ₃ ZnC@NC 10%	1	400	40	20000	13	93	2 h	⁵
Fe-Pt/CeO ₂	3	350	30	200000	21	100	200 h ^b	⁶
PtCuTe@UiO-67	3	400	20	24000	15.44	99.86	--	⁷
K-Cu/Al ₂ O ₃	3.8	280	30	4000	13.7	99	--	⁸
Ba-Cu/Al ₂ O ₃	3.8	280	30	4000	18.2	93.4	--	
2-K	3	400	30	720	20	100	40 h	⁹
K-WC/y-Al ₂ O ₃	3	300	20	4.8	100	--	--	¹⁰
K-WC ^c	3	350	20	3600	20.3	98.1	--	
Cu-ZnO	3	270	30	20000	5.3	93.2	--	¹¹
CuZnGaAlO ₂	3	270	30	20000	7.5	95.8	--	

Table S 3. Kinetic and adsorption constants, apparent activation energies and adsorption heats at T = 653 K.

	k ⁰ , K ⁰	Ea, ΔH (kJ mol ⁻¹)
k ₁ (mol g ⁻¹ h ⁻¹ bar ^{-1.5})	(3.89 ± 0.15) 10 ⁻²	97.3 ± 0.26
k ₂ (mol g ⁻¹ h ⁻¹ bar ^{-3.25})	(4.16 ± 0.56) 10 ⁻⁶	91.4 ± 0.23
k ₃ (mol g ⁻¹ h ⁻¹ bar ^{-2.75})	(1.35 ± 0.16) 10 ⁻⁶	37.9 ± 0.76
K _{H2} (bar ^{0.5})	(8.81 ± 0.17) 10 ⁻²	-49.9 ± 0.13
K _{H2O} (-)	(1.31 ± 1.24) 10 ¹	-37.2 ± 0.81
K _{CO} (bar ⁻¹)	(1.42 ± 0.69) 10 ⁻³	-11.2 ± 0.42

Table S 4. Other kinetic models studied in this work.

Power law	$r_{RWGS} = k_1 \left(p_{CO_2} p_{H_2} - \frac{p_{CO} p_{H_2 O}}{K_{eqRWGS}} \right)$
Xu-Froment's model	$r_{rwgs} = \frac{\frac{k_1}{p_{H_2}} \left(p_{CO_2} p_{H_2} - \frac{p_{CO} p_{H_2 O}}{K_{eqRWGS}} \right)}{\left(1 + K_{CO} p_{CO} + K_{H_2} p_{H_2} + K_{CH_4} p_{CH_4} + \frac{K_{H_2 O} p_{H_2 O}}{p_{H_2}} \right)^2}$
Hakeem-Alstrup-Weatherbee's model	$r_{rwgs} = \frac{k_1 \left(p_{CO_2} p_{H_2} - \frac{p_{CO} p_{H_2 O}}{K_{eqRWGS}} \right)}{\left(1 + K_{CO} p_{CO} + K_{H_2} p_{H_2} + K_{CO_2} p_{CO_2} + K_{H_2 O} p_{H_2 O} \right)^2}$

4. References

1. P. W. Readman and W. O'Reilly, *Journal of geomagnetism and geoelectricity*, 1972, **24**, 69-90.
2. J. Castells-Gil, S. Ould-Chikh, A. Ramírez, R. Ahmad, G. Prieto, A. R. Gómez, L. Garzón-Tovar, S. Telalovic, L. Liu, A. Genovese, N. M. Padial, A. Aguilar-Tapia, P. Bordet, L. Cavallo, C. Martí-Gastaldo and J. Gascon, *Chem Catal.*, 2021, **1**, 364-382.
3. L. Barberis, C. I. Versteeg, J. D. Meeldijk, J. A. Stewart, B. D. Vandegehuchte and P. E. de Jongh, *ACS Catal.*, 2024, **14**, 9188-9197.
4. M. Juneau, M. Vonglis, J. Hartvigsen, L. Frost, D. Bayerl, M. Dixit, G. Mpourmpakis, J. R. Morse, J. W. Baldwin, H. D. Willauer and M. D. Porosoff, *Energy Environ. Sci.*, 2020, **13**, 2524-2539.
5. N. E. C. Maluf, A. H. Braga, M. L. Gothe, L. R. Borges, G. A. S. Alves, R. V. Gonçalves, J. Szanyi, P. Vidinha and L. M. Rossi, *Eur. J. Inorg. Chem.*, 2021, **2021**, 4521-4529.
6. H. Wang, M. S. Bootharaju, J. H. Kim, Y. Wang, K. Wang, M. Zhao, R. Zhang, J. Xu, T. Hyeon, X. Wang, S. Song and H. Zhang, *J. Am. Chem. Soc.*, 2023, **145**, 2264-2270.
7. H. Zhang, H. Xu, Y. Li, X. Pan and L. Li, *Science China Materials*, 2020, **63**, 769-778.
8. A. Bansode, B. Tidona, P. R. von Rohr and A. Urakawa, *Catal. Sci. Technol.*, 2013, **3**, 767-778.
9. A. A. Isah, O. Ohiro, L. Li, Y. Nasiru, K. C. Szeto, P.-Y. Dugas, A. Benayad, A. De Mallmann, S. L. Scott, B. R. Goldsmith and M. Taoufik, *ACS Catal.*, 2024, **14**, 2418-2428.
10. J. R. Morse, M. Juneau, J. W. Baldwin, M. D. Porosoff and H. D. Willauer, *J. CO₂ Util.*, 2020, **35**, 38-46.
11. X. Liu, P. Ramírez de la Piscina, J. Toyir and N. Homs, *Catal. Today*, 2017, **296**, 181-186.